Plasma Catalysis

Sustainable Ammonia Synthesis from Nitrogen and Water by One-Step Plasma Catalysis

Tianqi Zhang [iD], *Renwu Zhou** [iD], *Shuai Zhang, Rusen Zhou, Jia Ding, Fengwang Li, Jungmi Hong, Liguang Dou, Tao Shao** [iD], *Anthony B. Murphy, Kostya (Ken) Ostrikov, and Patrick J. Cullen*

Sustainable ammonia synthesis at ambient conditions that relies on renewable sources of energy and feedstocks is globally sought to replace the Haber–Bosch process. Here, using nitrogen and water as raw materials, a nonthermal plasma catalysis approach is demonstrated as an effective power-to-chemicals conversion strategy for ammonia production. By sustaining a highly reactive environment, successful plasma-catalytic production of NH_3 was achieved from the dissociation of N_2 and H_2O under mild conditions. Plasma-induced vibrational excitation is found to decrease the N_2 and H_2O dissociation barriers, with the presence of matched catalysts in the nonthermal plasma discharge reactor contributing significantly to molecular dissociation on the catalyst surface. Density functional theory calculations for the activation energy barrier for the dissociation suggest that ruthenium catalysts supported on magnesium oxide exhibit superior performance over other catalysts in NH_3 production by lowering the activation energy for the dissociative adsorption of N_2 down to 1.07 eV. The highest production rate, 2.67 mmol $g_{cat.}^{-1}$ h^{-1}, was obtained using ruthenium catalyst supported on magnesium oxide. This work highlights the potential of nonthermal plasma catalysis for the activation of renewable sources to serve as a new platform for sustainable ammonia production.

T. Zhang, Dr. R. Zhou, Dr. R. Zhou, Dr. J. Ding, Dr. F. Li, Dr. J. Hong, Prof. P. J. Cullen
School of Chemical and Biomolecular Engineering, University of Sydney, Darlington, NSW 2008, Australia
E-mail: renwu.zhou@sydney.edu.au
Dr. S. Zhang, Dr. L. Dou, Prof. T. Shao
Beijing International S&T Cooperation Base for Plasma Science and Energy Conversion, Institute of Electrical Engineering, Chinese Academy of Sciences, Beijing 100190, China
E-mail: st@mail.iee.ac.cn
Dr. R. Zhou, Prof. K. Ostrikov
School of Chemistry and Physics and Centre for Materials Science, Queensland University of Technology, Brisbane, Qld 4000, Australia
State Key Laboratory of Electrical Insulation and Power Equipment, Center for Plasma Biomedicine, Xi'an Jiaotong University, Xi'an 710049, China
Dr. A. B. Murphy
CSIRO Manufacturing, Lindfield, NSW 2070, Australia

[iD] The ORCID identification number(s) for the author(s) of this article can be found under https://doi.org/10.1002/eem2.12344.

1. Introduction

Ammonia is one of our most important synthetic chemicals. It sustains global food production and is a potential carbon-free vector for storing and transporting hydrogen.[1,2] The Haber–Bosch (H-B) process ($N_2 + 3H_2 \rightarrow 2 NH_3$), which dominates ammonia synthesis, requires high temperatures and pressures, an ultrapure H_2 feed, and large centralized production plants to achieve economic viability (**Figure 1**a). The hydrogen is currently almost exclusively derived from the reforming of fossil hydrocarbons, which results in annual CO_2 emissions of 300 Mt,[3] ~1.5% of all greenhouse gas emissions.[4] A green alternative, for example, a process that enables carbon-neutral and decentralized ammonia production using water as the hydrogen feedstock and powered by renewable energy sources, is urgently required.[5,6]

Photochemical and electrochemical routes have been devised for ammonia synthesis from N_2 and H_2O under mild conditions.[7–10] The focus of these studies lies on the suppression of the competing hydrogen evolution reaction to improve selectivity toward N_2 reduction and/or the design and selection of desirable catalysts to achieve the goal. However, the electrons transferred to N_2 molecules in photocatalysis and electrocatalysis cannot provide sufficient energy to break the strong N≡N bonds (bond energy of 945 kJ mol^{-1}). As a result, the production rate of ammonia is prohibitively low (Figure 1b).

Gas discharge plasmas with highly energetic electrons, generated by applying electrical energy to a feeding gas, are capable of activating inert N_2 molecules into more reactive, vibrationally or electronically excited states to promote dissociation of nitrogen molecules, and thus, facilitate the breaking of ultrastable N≡N bonds.[9,11–13] Typically, for nonthermal plasma (NTP), the energy introduced mainly heats the electrons, creating a thermal nonequilibrium, energy-efficient and highly reactive environment suitable to couple with catalysts (termed plasma catalysis), allowing thermodynamically unfavorable reactions to proceed under ambient conditions.[14,15] Also, similarly to electrocatalysis, NTP can be powered by renewable electricity.[16] NTP has demonstrated encouraging yields of ammonia; however, the hydrogen species in these reports comes from high-purity H_2, which is obtained from cost-demanding electrocatalytic hydrogen evolution reactions
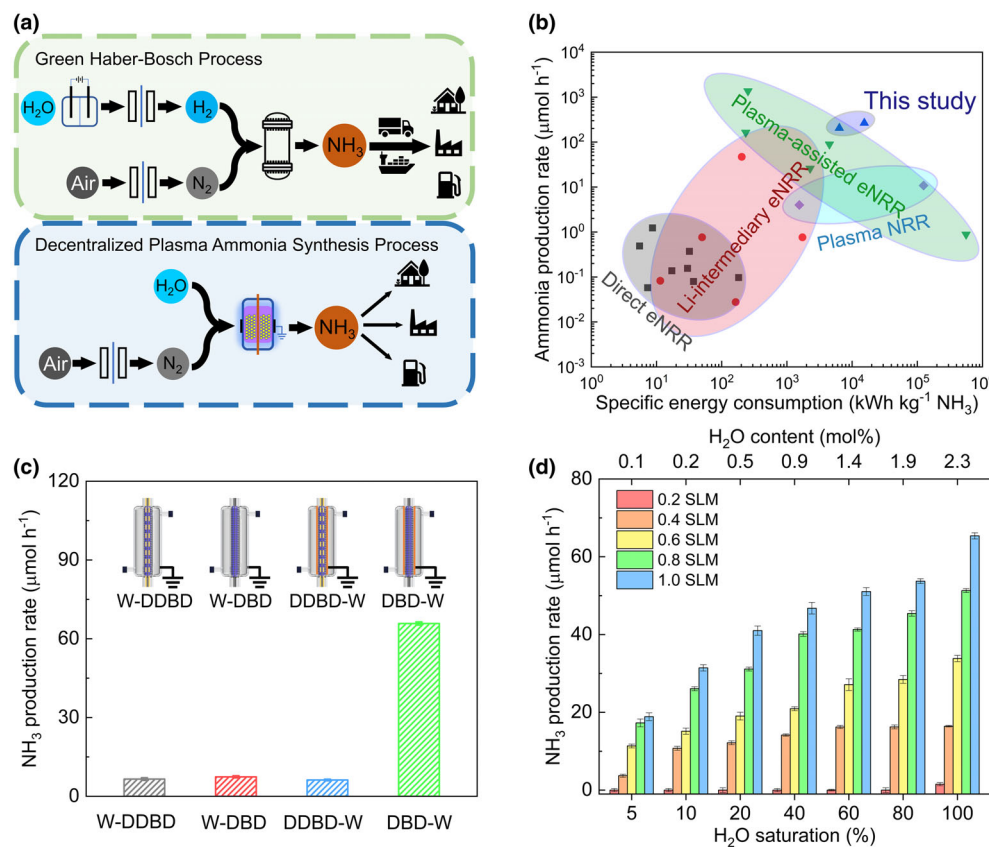
Figure 1. Plasma reactor designs and performance. a) Schematic illustration of centralized green Haber–Bosch process and proposed decentralized plasma ammonia synthesis process. b) Comparison of NH₃ production performance in direct electrochemical nitrogen reduction reaction (eNRR) (black square, gray area), Li-intermediary eNRR (red dot, yellow area), plasma-assisted eNRR (green triangle, green area), and plasma nitrogen reduction reaction (NRR) systems (cyan rhombus, cyan area). Table S1 provides detailed information.[7] c) Influence of reactor design on NH₃ synthesis rate. d) NH₃ synthesis rate in the single dielectric barrier discharge—water-cooled (DBD-W) system as a function of H₂O vapor saturation for different N₂ flow rates.

and some challenging process conditions (e.g., low pressure, high temperature, or high gas flow rate) may primarily hinder the upscaling of this technology and bring some inevitable environmental challenges.

In our study, we demonstrate a more straightforward one-step process, where both the water dissociation and nitrogen activation are driven by the atmospheric NTP under ambient pressure and temperature. Experiments were performed for different reactor configurations, catalysts, discharge powers, and gas flow rates with different H₂O vapor saturations. An optimized configuration of an advanced plasma reactor, packed with a ruthenium (Ru) catalyst, was found to achieve an ammonia production rate of 2.67 mmol $g_{cat.}^{-1}$ h^{-1}. By using spectroscopic and theoretical studies, we elucidate that the high ammonia production is a result of the efficient dissociative adsorption of H₂O and vibrationally excited N₂(v) by the plasma–catalyst interactions, predominantly through Eley–Rideal (E-R) reactions.

2. Results

2.1. Plasma Reactor Designs and Explorations

We begin by studying the effect of the plasma reactor features on the ammonia production rates. Four different reactor configurations (Figure S1) are developed: a water-grounded double dielectric barrier discharge (W-DDBD), water-grounded single dielectric barrier discharge (W-DBD), double dielectric barrier discharge—water-cooled (DDBD-W), and single dielectric barrier discharge—water-cooled (DBD-W). The configuration markedly affects the NH₃ synthesis performance (Figure 1c). While the W-DDBD, W-DBD, and DDBD-W reactors show similar ammonia synthesis rates (7.0–9.0 μmol h^{-1}), the DBD-W reactor using a copper foil sheet as the ground electrode instead of water leads to a significant increase in the NH₃ synthesis rate by a factor of ~10 (65.5 μmol h^{-1}). The electrical characteristic measurement results (Figure S2) show that DBD-W configuration provides a highly enhanced current response, which leads to desirable plasma conditions with a significantly increased electron density and minimized NH₃ dissociation in the gas phase by high-energy electrons,[21] in comparison to the other three DBD reactors (Figure S3). Therefore, the remaining studies are performed based on the DBD-W reactor. We investigate the effect of the feeding gas flow rates and the water vapor content on the NH₃ production in the DBD-W system. Increasing the gas flow rate results in an improved NH₃ synthesis rate (Figure 1d): the rate increasing from 1.53 to 65.4 μmol h^{-1} for gas flow rates rising from 0.2 to 1.0

(HERs) or carbon-intensive reforming processes.[17,18] Substitution of H₂O for H₂ is the key to make NTP-enabled ammonia synthesis sustainable. Understanding the molecular-level mechanisms of the synergetic effects of plasma–catalyst interactions for ammonia from N₂ and H₂O is crucial for next-step studies.

Recently, the plasma-electrochemical integrated systems have been proposed as an alternative way for nitrogen reduction using N₂ and H₂O. In these systems, the plasma is utilized for nitrogen activation, which subsequently lowers the energy barrier to initiate electrochemical processes for nitrogen fixation. One study of significant advance to our study developed a continuous and scalable plasma-electrochemical hybrid technology for sustainable and facile production of ammonia via a NOx intermediary approach, with a world-leading production rate of green ammonia yielding 23.2 mg h^{-1} (3.95 g kWh^{-1}).[7] Sharma et al.[19] established a plasma-assisted electrochemical approach, in which the hydrogen production (from water oxidation) and nitrogen activation (by the low-pressure plasma at 500 °C) were separated, with an energy efficiency of 0.101 g kWh^{-1}. More recently, Muzammil et al.[20] developed a hybrid plasma-thermal catalytic system, combing a plasma-enabled NOx production and a thermal catalysis process, with a relatively high gas flow rate of N₂ (20 L min^{-1}) but a high energy efficiency (2.94 g kWh^{-1}). Nevertheless, the relative complexity of the systems

standard liter per minute (SLM), at 100% H_2O saturation. Higher H_2O vapor contents also lead to higher production rates of NH_3.

To further improve the NH_3 production rate, a model Ru catalyst—the most active metal catalyst in the H-B process—is packed into the discharge area. Different oxides (i.e., Al_2O_3, SiO_2, MgO) were tested as supports. Catalyst characterization results, including TEM, XPS, XRD, and NH_3-TPD, are shown in Figures S4–S6. Compared to other metal oxide supports (Al_2O_3 and SiO_2), MgO with strong basicity enhances the N_2 dissociation rate by donating sufficient number of electrons to lower the dissociation barrier and thereby improve the ammonia synthesis rate, which is consistent with our results in **Figure 2**. In contrast, the Al_2O_3-packed case only produces a relatively small amount of ammonia, possibly due to the significantly lower electron density, which leads to a lower concentration of active radicals, atoms, and ions than the other oxide cases (Figures S7 and S8). The competition with N (s) hydrogenation by the strong interrupting effect of surface-adsorbed oxygen species, and a slower desorption of ammonia from the alumina surface because of relatively strong binding are other possible reasons.[22] NH_3-TPD measurement results (Figure S6B) show the high density of strong acid sites on the Al_2O_3 surface in comparison to the other supports, leading to a slight reduction of NH_3 yield.[21,23] The presence of Ru supported on these oxides, especially on MgO, markedly enhances the synthesis rate to 2661 μmol $g_{cat.}^{-1}$ h^{-1} (Figure 2a). Electrical measurements of the DBD reactor coupled with various catalysts show that the packing catalysts can provide higher electron density and electron energy than the plasma-only (N_2/H_2O) case. All QV Lissajous figures (Figure S7) for various catalysts at the same input conditions

(discharge voltage V_{p-p}: 9.08 kV for MgO, 8.27 kV for SiO_2, 7.86 kV for Al_2O_3, 8.23 kV for Ru/MgO, 9.15 kV for Ru/SiO_2, and 10.57 kV for Ru/Al_2O_3) show a similar typical parallelogram shape, indicating that the plasma properties do not change significantly using the same electrode configuration, which is consistent with other studies.[24]

The NH_3 synthesis rate increases with the specific energy input (SEI) (Figure 2b). SEI is adjusted by varying the discharge power at a constant gas flow rate of 1.0 SLM. Specifically, the NH_3 synthesis rate increases from 2050 to 2661 μmol $g_{cat.}^{-1}$ h^{-1} when the SEI increases from 1.33 to 4.20 kJ L^{-1} in the presence of the Ru/MgO catalyst. However, the energy efficiency of ammonia synthesis decreases with increasing SEI (Figure S9). This may be attributed to the fact that increasing the SEI shifts the electron energy distribution function to higher energies, leading to an increased probability of ionization and dissociation reactions, which consume much energy. The lowest energy pathway is vibrational excitation of molecules followed by dissociative adsorption on the catalyst surface. The catalysts show a stable NH_3 production rate over a 5-h period (Figure 2c), and the main physicochemical properties of the catalysts remain unchanged (Figure S4). The NH_3 synthesis rate and the energy efficiency of Ru/MgO remain constant over five reuse cycles (Figure 2d), suggesting the long-term stability of the catalysts under the N_2 and H_2O reactions. A further comparison of the physicochemical properties of the fresh and spent catalysts, as determined by N_2-BET and XPS measurements (Figures S4 and S5), also suggests that the reactions in plasma do not have a significant impact on the catalyst structures and surfaces.
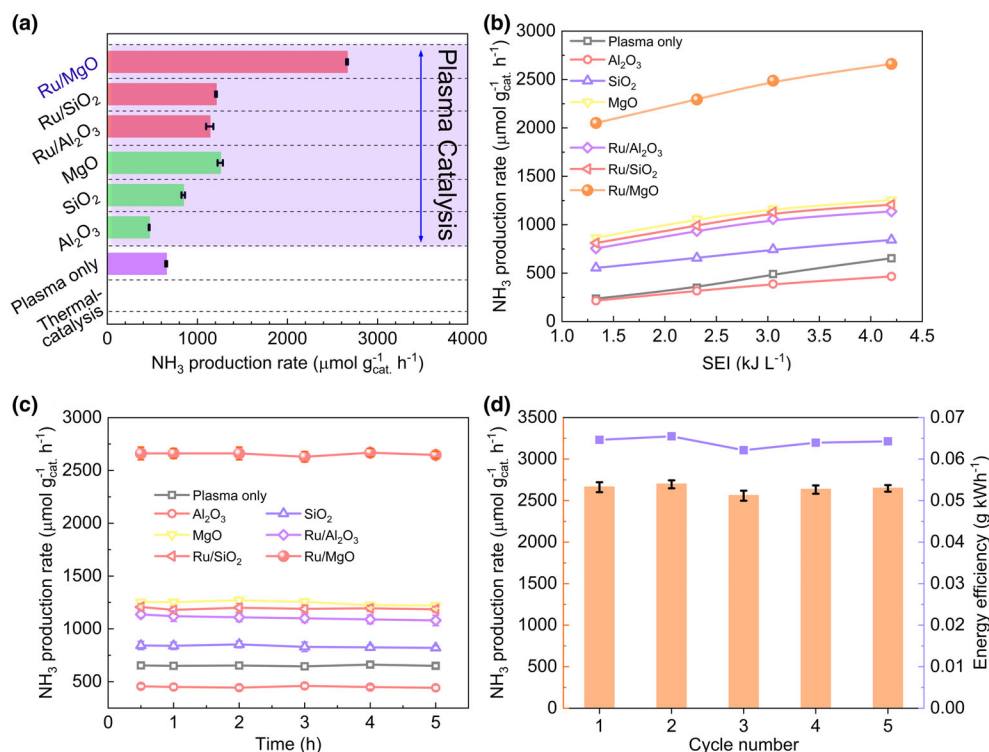
2.2. Gas-Phase Plasma Chemistry and Computational Simulations

Next, we seek to provide insights into the mechanism of the plasma-enabled catalytic activation of N_2 and H_2O to NH_3. Optical emission spectroscopy (OES) is first performed to study the plasma excitation process in the absence of the catalysts (Figure S10). OES indicates that plasma-activated nitrogen species exist in the form of vibrational and rotational excitation, electronic excitation, and ionization without dissociation being observed (Figure S10A). The second positive bands of N_2 ($C^3\prod_u \rightarrow B^3\prod_g$) in the spectra indicate the presence of electronically excited nitrogen molecules, while the existence of N_2^+ ($B^2\sum_u^+ \rightarrow X^2\prod_g^+$) first negative system (FNS) demonstrates the ionization of N_2 molecules (Figure S10A,D). Unlike a N_2/H_2 system reported in the literature,[23] N and H emission lines are not observed in our N_2/H_2O system, possibly

Figure 2. Catalyst evaluation for ammonia synthesis. a) NH_3 synthesis rates at a specific energy input (SEI) of 4.20 kJ L^{-1} for thermal catalysis (without plasma) operated in a tube furnace at 200 °C and for plasma-only and plasma catalysis (1.0 SLM, 100% RH). b) NH_3 synthesis rates as a function of SEI using different catalysts. c) Catalyst stability tests. d) NH_3 synthesis rates and energy efficiencies for reused Ru/MgO with an SEI of 4.20 kJ L^{-1}.

due to the strong dissociative attachment of electrons to H_2O molecules, causing a reduction in electron density (Figure S8). However, NO bands ($A^2\Sigma \rightarrow X^2\Pi$) are visible from 200 to 300 nm (Figure S10B) and the NH ($A^3\Pi \rightarrow X^3\Sigma^-$) line at 336.1 nm is observed as a preshoulder to the N_2 (0,0) peak at 337.1 nm (Figure S10C). The normalized intensities for N_2^+ and NH are higher for the Ru/MgO catalyst than the other supports and catalysts (Figure S11), indicating that Ru supported on magnesium oxide can promote the generation of more excited species and radicals.

The spectra of the second positive bands of N_2 ($C^3\Pi_u \rightarrow B^3\Pi_g$) are fitted to calculate the vibrational (T_{vib}) and rotational temperatures (T_{rot}). T_{vib} values obtained from the pure N_2 and N_2/H_2O plasma are 2400 and 2020 K, respectively. These data indicate that the presence of H_2O vapor causes the quenching of N_2 vibrational levels, which can be a result of N_2/H_2O vibrational–translational relaxation.[25] Electron-induced inelastic collisions and vibrational–vibrational energy transfer can shift the vibrational energy distribution of N_2(v) to a higher vibrational temperature, significantly higher than the bulk gas temperature. Using the vibrational temperature obtained from the N_2/H_2O plasma (T_{vib} (N_2) = 2020 K), the Treanor distribution technique is applied to obtain an estimate of the non-Boltzmann population densities of the vibrationally excited N_2 states (Figure S12). The Treanor distribution indicates that the fraction of N_2 in the first vibrationally excited state is ~14.4%, while the high-lying vibrationally excited states (v_4–v_6) have low fractions of ~0.1%. T_{vib} (N_2) values increase slightly to 2350 K in the presence of the oxide supports and further to ~2600 K when Ru is introduced (**Figure 3**a). Similar T_{vib} levels (equivalent to the vibrational energy of excited N_2) indicate that the introduction of Ru and oxide supports does not change the excitation pattern of N_2 in the gas phase and thus, the difference in the observed ammonia production with different catalysts does not come from changes in the vibrational energy of N_2.

We then quantify, by plotting the electron loss fraction (Figure 3b) and electron collision rate coefficients (Figure S13) of electron-induced reactions (Table S3) as a function of the reduced electric field (E/N), the energy transfers to excitation, ionization, and dissociation channels of both N_2 and H_2O. When the E/N ratio is between 80 and 100 Td as applies to our experimental conditions, most of the energy loss goes into vibrational excitation of the N_2 and H_2O molecules in the gas phase, while the electronic excitation and ionization channels only dominate over 100 Td. We further use density functional theory (DFT) to understand the reaction process. All three oxides show similar energy profiles toward N_2 activation with a prohibitively high energy barrier of >7 eV for the dissociation of adsorbed N_2 (Figure 3 c), indicating that the supports may not provide any surface-adsorbed N(s) through the dissociative adsorption of N_2 molecules. Instead, direct adsorption of nitrogen atoms is considered to be the only pathway to produce N(s) and mostly subsequent E-R (Eley–Rideal) interaction contributes to NH_3 production with enhanced plasma properties by dielectric material packing.[24,26] Unlike these oxides, the Ru cluster on the MgO surface shows a much stronger adsorption of N_2 (−1.95 eV) as compared to −0.75 eV for Ru/SiO_2 and −1.33 eV for Ru/Al_2O_3, and the dissociation has only a low barrier of 1.07 eV along with an exothermic process of 0.33 eV. This higher activation energy for the hydrogenation of surface-adsorbed N(s), NH_x(s) species can impact the NH_3 production, which may lead to a decreased production rate of L-H (Langmuir–Hinshelwood) interaction (NH_2(s) + H(s)) to form NH_3(s) on the surface. Instead, the production of NH_3 by E-R (Eley–Rideal) interaction such as from H_2 + NH(s) or H + NH_2(s) becomes more important (Figure S14). Moreover, these results demonstrate the strong N_2 dissociation ability of the Ru/MgO catalyst. The high activity of Ru/MgO can be clearly evidenced by the enlarged bond length of N–N (Figure 3c). The full reaction pathway for Ru/MgO indicates that the hydrogenation of surface-adsorbed NH_2(s) to form NH_3(s) on the surface is the most energy-intensive elementary step, with an endothermic requirement of 0.68 eV (Figure S14).

3. Discussion

Here, we demonstrate a NTP catalysis approach for ammonia synthesis using nitrogen and water vapor as raw materials. The performance of the plasma-enabled ammonia
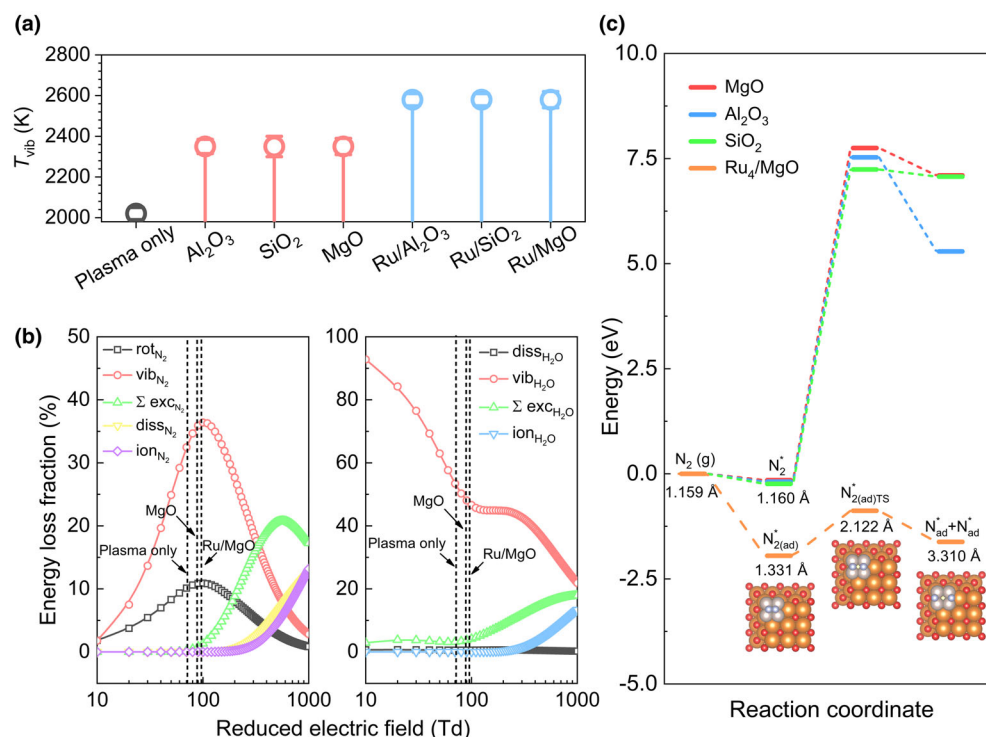
Figure 3. Plasma-induced N_2 activation and energy diagram of N_2 dissociation. a) Vibrational temperature of N_2 without or with the addition of different catalysts. Estimated electron energy distribution function of the N_2/H_2O plasma. b) Electron energy loss fractions. c) N_2 dissociation process over different catalysts.

synthesis is strongly dependent on the design of the DBD reactor, with the DBD-W configuration operating with a ground mesh electrode cooled through the use of a jacketed glass water-based heat exchanger showing a remarkable improvement in ammonia production. The estimated electron energies and densities (Figure S3) show significant differences in the four DBD configurations used in this work. The DBD-W reactor provided currents and electron densities 1.4–1.6 times higher than the other three reactors. Considering the predominant dissociation mechanism of NH_3 is via high-energy electrons,[21] low-energy electron distribution characteristics may be beneficial to minimize the loss rate of the produced ammonia molecules in the gas phase. By using the Boltzmann equation solver BOLSIG+, we show that the DBD-W can generate high densities of vibrationally excited $N_2(v)$ and $H_2O(v)$ (Figure S13), which can lead to a high reaction rate of dissociative adsorption for the efficient production of N(s) and H(s), as Mehta et al. suggested.[11]
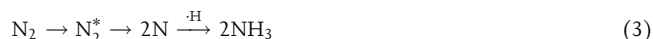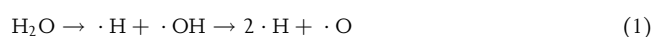
It is important to note that the high density of electrons contributes to gas heating and a wall temperature increase, which can significantly influence the catalytic synthesis process. The possible mechanisms include elastic electron collisions with heavy particles, electron–ion recombination, and excitation of molecules into high vibrational and rotational energy states followed by fast relaxation process such as vibrational–translational and rotational–translational relaxation.[26] The measured surface temperature of the different reactor configurations supports the importance of gas heating from high-density electrons and the relaxation process of vibrationally excited species. Both W-DBD and W-DDBD employ the water as the ground electrode, which effectively maintains the outer-wall temperature of the reactor at around 30 °C. The DDBD-W reactor has a copper mesh as the ground electrode, but the presence of dielectric barrier surrounding the high-voltage electrode also contributes to a relatively low wall temperature (~65 °C). In contrast, the DBD-W configuration shows a significantly higher outer-wall temperature (~200 °C), which indicates a high gas temperature. The high gas temperature will accelerate gas-phase and surface reactions, in particular desorption of the surface-adsorbed NH_3.[27] As the conversion of N_2 and H_2O to ammonia is an endothermic reaction, the higher operating temperature of the DBD-W reactor, which leads to a higher initial reactant energy, is preferred for the reaction. Therefore, the gas and surface temperatures, which depend strongly on the reactor design, are crucial factors for the effective synthesis of ammonia in a plasma-driven N_2/H_2O system at atmospheric pressure.[11,27–29]

In considering the catalyst, it is worthwhile to comment that the DBD plasma, with a relatively low degree of dissociation and a high degree of excitation (vibrational or electronic), typically requires a noble active metal for dissociative adsorption of N_2,[30] since N_2 is not fully dissociated in the plasma environment. Ru has a very low dissociation energy barrier for water (0.5–0.8 eV),[31] as well as for N_2, which has been confirmed with our DFT calculations. The low energy barrier for water is beneficial for the efficient production of surface-adsorbed H(s), which is crucial for ammonia production, especially with the limited hydrogen sources in the N_2/H_2O system. Considering almost the identical plasma characteristics when Ru catalyst is added to the oxide support, the reason for the further improvement in ammonia production, particularly with the combination of Ru/MgO, can be related to the improved electron transfer from the support to the surface-adsorbed species and the different bonding energy of surface-adsorbed nitrogen adatom as Kitano et al. suggested.[32] In addition, as also confirmed in Mehta et al.'s study,[11] Ru can provide a high synthesis rate of ammonia for both step and terrace sites when the plasma
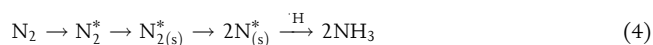
is present, which demonstrates its suitability for plasma synthesis as well as the conventional thermochemical process. In a systematic study, Aika et al. demonstrated the high activity of Ru/MgO compared to other metal oxides such as CaO, Al_2O_3, and TiO_2.[33] This was attributed to the strong basicity of MgO, which can provide a high surface charge density of Ru for electron donation to activate dinitrogen molecules during ammonia synthesis.[34,35]

The turnover frequencies (TOFs) for all the catalysts were determined to evaluate the catalytic performance (Figure S15). The TOF value in the Ru/MgO system is around 7.41×10^{-2} to 8.27×10^{-2} s^{-1} at the SEI of 1.33–4.20 kJ L^{-1}, which is more than 10 times higher than that of Ru/SiO$_2$ and Ru/Al$_2$O$_3$ catalysts. Moreover, this TOF value from our work is comparable or even higher than values obtained in other works using similar plasma-catalysis systems for ammonia synthesis. For example, Wang et al.[23] achieved 2.16×10^{-3} s^{-1} using Ni/Al$_2$O$_3$ in a H_2/N_2 DBD system. Mehta et al.[11] used a microkinetic model to calculate the ammonia synthesis TOFs at Ru terrace sites and step sites of around 10^{-5} to 10^{-6} s^{-1} when the plasma is turned on. The introduction of a catalyst to the discharge zone significantly enhanced the production of ammonia (Figure 2), indicating the existence of plasma-assisted surface reactions in addition to the gas-phase reactions. A schematic illustration of ammonia synthesis on catalyst surfaces in the plasma-catalytic N_2/H_2O process is shown in **Figure 4**a. The presence of the catalyst facilitates the dissociation of the plasma-generated species. One of the key mechanisms is that plasma-induced vibrationally excited $N_2(v)$ species can be adsorbed on the catalyst surfaces and efficiently dissociated to form N(s) on the catalyst surface with a higher reaction rate than the ground-state $N_2(X)$.[11,30] A possible pathway to produce NH_3 in the N_2/H_2O system is shown with the following four general steps: 1) excitation/ionization of nitrogen and water molecules (Equations 1–3); 2) formation of the gaseous reactive species and NH_3 molecules by chemical reactions in the gas phase; 3) surface adsorption of reactive gas species (Equation 4); 4) production of ammonia through E-R (Eley–Rideal) or L-H (Langmuir–Hinshelwood) mechanism as commonly postulated in publications on the N_2/H_2 system.[21,28,36,37]
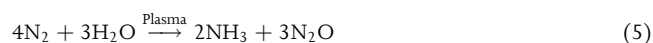
Gas Phase:

$$H_2O \rightarrow \cdot H + \cdot OH \rightarrow 2 \cdot H + \cdot O \tag{1}$$

$$N_2 \rightarrow N_2^* \xrightarrow{\cdot O} N_2O \tag{2}$$

$$N_2 \rightarrow N_2^* \rightarrow 2N \xrightarrow{\cdot H} 2NH_3 \tag{3}$$

Catalyst Surface:

$$N_2 \rightarrow N_2^* \rightarrow N_{2(s)}^* \rightarrow 2N_{(s)}^* \xrightarrow{\cdot H} 2NH_3 \tag{4}$$

Overall:

$$4N_2 + 3H_2O \xrightarrow{Plasma} 2NH_3 + 3N_2O \tag{5}$$

The performance and energy efficiency achieved in our work are also compared with other studies on NH_3 production in N_2/H_2O plasma systems (Table S1). The conversion of N_2 under all conditions remained rather low, as is common for N_2/H_2O plasma systems.[9,19,38–42] The highest conversion observed in our proposed

system corresponds to the case when Ru/MgO was used, reaching a maximum of 0.0297% (Table S2), which is considerably higher than other N_2/H_2O plasma systems.[9,19,38–42] The reported ammonia production rate and energy efficiency in N_2/H_2 plasma discharges range from 100 to 1000 {mol $g_{cat.}^{-1}$ h^{-1}, 1–36 g NH_3 kWh^{-1}.[26,43] The energy cost of hydrogen production in the commercial Haber–Bosch process is primarily from the energy-intensive methane reforming process at 800–1000 °C.[26,44] In addition, the produced H_2 must be stored and delivered, posing potential safety issues. Therefore, replacing H_2 with H_2O to supply hydrogen is a significant benefit without an extra energy-intensive conversion process. In contrast, our approach demonstrates a more straightforward one-step process, where both the water dissociation and nitrogen activation are driven by the atmospheric NTP catalysis to give the remarkable ammonia synthesis rate reported for N_2/H_2O-based plasma synthesis of ammonia (Table S1). Further improvements in energy efficiency are foreseeable in our system, considering the small amount of the catalyst material used and the feasibility of combining with the already demonstrated approaches such as utilizing renewable energy sources and applying short pulse power sources.

A challenge of using H_2O to replace H_2 in plasma ammonia synthesis is the formation of oxidative species, resulting in the oxidation of some nitrogen species. Here, the main NO_x product is nitrous oxide (N_2O) with a selectivity of over 99% (Equation 4), while the concentrations of other nitrogen oxides (N_xO_y) are below the detection limits. Compared with plasma-only experiments, catalyst-packed DBD processes do not change the concentration of N_2O significantly, suggesting its production occurs predominantly in the gas phase (Figure 4b). To make full use of plasma-excited nitrogen, we devised a concept for the comprehensive production of ammonia, powered fully by electricity, as illustrated in Figure 4d. The process starts with the membrane separation of air to generate pure N_2 for plasma activation in the presence of

water vapor. The NH_3 formed by the process is, after liquefaction, ready to use. The remaining N_2 and N_2O are separated and transferred into a recycle loop and to an oxidation process, respectively. Because of the high selectivity of nitrogen oxidation products ($N_2O > 99\%$), it can also be directly output as a product or as a reactant for other chemical synthesis.

A zero-dimensional (0D) plasma kinetic model reveals the important chemical pathway to produce ammonia in the N_2/H_2O system. The description of the kinetic model and data are given in Figure S16. As shown in Figure 4c, the high-energy electrons initiate plasma catalysis by producing high-density $N_2(v)$, and a significant fraction of the $N_2(v)$ (87.5%) contributes to the production of the surface-adsorbed N (s). Afterward, as discussed earlier and confirmed by the DFT results, ammonia production predominantly proceeds through E-R interactions such as the interaction of NH(s) and H_2 or $NH_2(s)$ and atomic H rather than the L-H interaction between $NH_2(s)$ and H(s) due to the high activation energy for the hydrogenation reaction on Ru/MgO surface. Although the optical emission from the excited states of N and H atoms is not observed, the role of atomic species and radicals in the gas phase cannot be neglected. Since hydrogen species involved in the reaction can only be generated from the decomposition of the limited supply of water molecules, the increased input flow rate of temperature-controlled water vapor results in an enhanced NH_3 production rate, with 2 times higher values obtained at an increased water vapor supply (7.4% at 40 °C). While optimization will require further studies, our findings have shown that increasing the H_2O content in the gas phase contributes to a higher yield of ammonia for given plasma characteristics.

We also observed zero ammonia formation in a N_2/H_2O reaction using a conventional thermal–catalytic approach (200 °C) with the employment of the same catalysts and by thermal equilibrium calculations (Figure 2a and Figure S17), which indicates that the high-energy electrons generated under NTP conditions are involved in the reaction
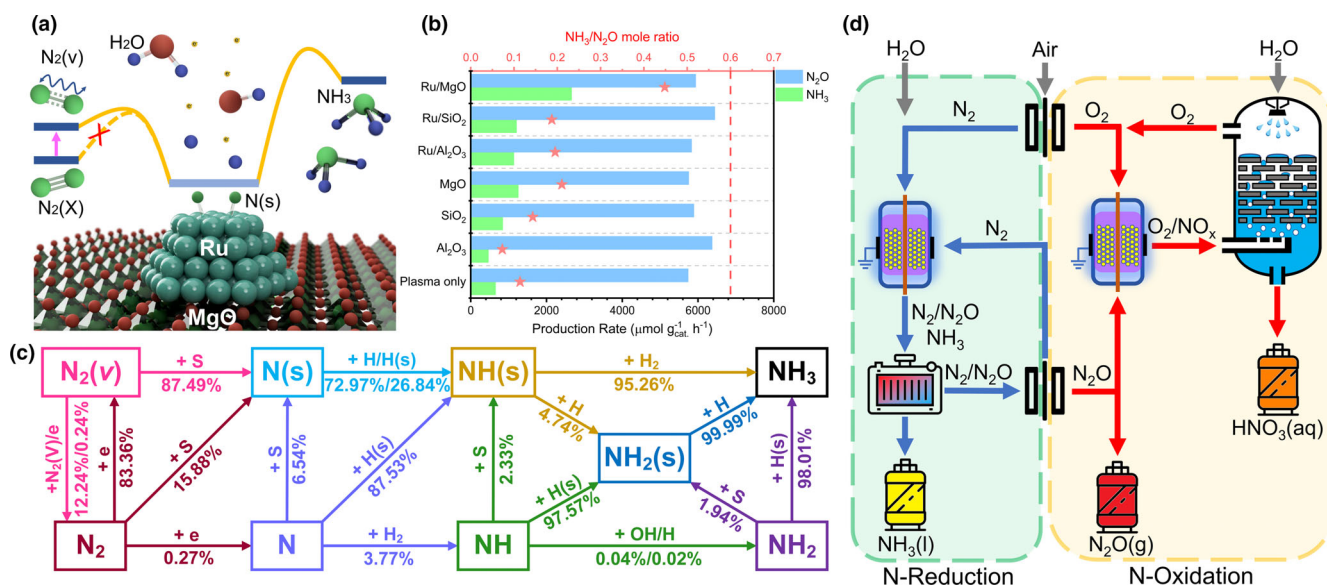

Figure 4. NH_3 formation reactions and NO_x production in the plasma-catalytic system. a) Schematic illustration of sustainable plasma-catalytic synthesis of ammonia from N_2 and H_2O on Ru-doped MgO surface. b) Summary of the generation rates of NH_3 and N_2O over different catalysts. c) Possible major reaction pathways for plasma-catalytic ammonia synthesis of N_2/H_2O system. Important paths and reaction rates are shown in Figure S15. d) Proposed sustainable ammonia production process. Part I: nitrogen reduction and ammonia production (blue lines and green region). Part II: nitrogen oxidation and nitric acid production (red lines and orange region).

and reduce the overall energy barrier for NH_3 synthesis. Our DFT simulations clarify the reaction pathway of NH_3 synthesis, N_2 activation, and the corresponding energy profiles under NTP conditions. The formation of chemisorbed N(s) at the Ru site has only a low barrier of 1.07 eV along with an exothermic process by 0.33 eV, allowing significantly enhanced N_2 dissociation on Ru/MgO catalyst. Recent studies describe a "hot-atom" mechanism in which the energy released in the adsorption process is used to elevate the vibrational energy level of molecules, which may promote the dissociation of N_2 at the catalyst surface.[45,46] In this study, the plasma-induced vibrational excitation is found to decrease the N_2 and H_2O dissociation barriers, with the presence of matched catalysts in the NTP discharge reactor contributing significantly to molecular dissociation on the catalyst surface ruthenium catalysts supported on magnesium oxide exhibit superior performance over other catalysts in NH_3 production by lowering the activation energy for the dissociative adsorption.

4. Conclusion

In summary, this work presents a plasma-catalysis avenue that enables ambient ammonia synthesis directly using renewable sources: N_2, H_2O, and electricity. Through process designs and computational studies on catalytic activity, our innovation is leaping the "unfavorable" reaction toward favorable ammonia production. A high rate of ammonia production (2.67 mmol $g_{cat.}^{-1}$ h^{-1}) has been demonstrated with a low activation energy of dissociative adsorption of N_2 on the catalyst surface, paving a new way for supplementing the Haber–Bosch process. This progress in sustainable ammonia synthesis only requiring nitrogen and water is expected to set a new benchmark for sustainable ammonia synthesis and to be a precursor to lead further innovation in broad plasma-catalysis research.

5. Experimental Section

Nessler's reagent, sulfuric acid (H_2SO_4, 98%), potassium hydroxide (KOH, ≥85%), ammonia sulfate ((NH_4)$_2SO_4$, ≥99.0%), magnesium oxide (MgO, fused, 150–325 mesh, ≥95%), fused silica (SiO_2, powder, 0.2–0.3 μm aggregate), aluminum oxide (Al_2O_3, activated, neutral, 0.05–0.15 mm), triruthenium dodecacarbonyl ($Ru_3(CO)_{12}$, 99%), and tetrahydrofuran (≥99.0%) were purchased from Sigma-Aldrich and directly used without further purification. Nitrogen gas (grade 5.0, 99.999%) was purchased from BOC, Australia.

Synthesis of Ru-doped metal oxide catalysts: Commercial fumed silica (SiO_2), activated aluminum oxide (Al_2O_3), and magnesium oxide (MgO) were used as supports for the preparation of Ru catalysts. Triruthenium dodecacarbonyl ($Ru_3(CO)_{12}$, 99%) and tetrahydrofuran (≥99.9%) were used as an Ru precursor and solvent, respectively. The Ru catalysts were prepared by the incipient wetness impregnation method. First, $Ru_3(CO)_{12}$ was dissolved in tetrahydrofuran under stirring to form a clear solution containing 0.5 wt.% Ru. Then, the solution was added to the supports. The mixture was ultrasonically treated for 10 min and subsequently dried in an oven at 60 °C for 2 h. An overall Ru content of 5 wt.% was achieved by repeated impregnation and drying. The powder was treated in a tube furnace at 500 °C for 2 h with a heating rate of 2 °C min^{-1} under H_2 flow (50 mL min^{-1}).

DBD plasma reactor: The experimental setup is shown in Figure S1A. The main experiments were conducted using a separated-cooling plasma reactor with coaxial stainless steel rod electrode and quartz tube with copper mesh grounding (DBD-W). An industrial chiller (with recycled water at 20 °C) was used to maintain the reactor in a stable temperature environment. The humidity of inlet nitrogen gas was controlled by a water-filled Drechsel flask and two separate mass flow meters which split the gas flow and merge again into the plasma reactor. The total

N_2 flow rate was varied from 0.2 to 1 SLM. The concentration of H_2O vapor is quoted in percentage of the relative saturation at 20 °C (ambient temperature during the experiments), and in molar percentage as calculated from the relative saturation. Thermal catalytic experiments were conducted by the setup shown in Figure S1B. Humidified N_2 (1 SLM, 100% H_2O saturation) was streamed through the packed catalyst (100 mg) quartz tube (8 mm ID, 10 mm OD, 300 mm length) in the tube furnace where the temperature was set at 200 °C.

In the experiment, W-DBD and DBD-W used a stainless steel electrode (6.0 mm OD, 250 mm length), while W-DDBD and DDBD-W used a quartz-covered stainless steel electrode (quartz: 4.0 mm ID, 6.0 mm OD, 200 mm length; steel electrode: 4.0 mm OD, 250 mm length). All reactors used quartz tubes (8.0 mm ID, 10.0 mm OD, 300 mm length). W-DDBD and W-DBD reactors used all-in-one quartz cooling jacket (30.0 mm OD, 68.0 mm length), while DDBD-W and DBD-W reactors used a separate quartz cooling jacket (11.6 mm ID, 34.0 mm OD, 68.0 mm length). A tungsten needle (2.0 mm ID, 30 mm length) for grounding was immersed in the cooling water of an all-in-one quartz cooling jacket for the W-DDBD and W-DBD reactors. A copper mesh (68 × 180 mm dimension, 0.4 mm thickness) was placed between the quartz tube and quartz cooling jacket and grounded in the DDBD-W and DBD-W reactors. For plasma-catalysis experiments, quartz wool was wrapped underneath the plasma zone to support the packed catalysts (100 mg). The plasma AC power supply used in this study is CTP-2000K from Suman (Nanjing, China), capable of generating 0–30 kV AC voltage in a range of 1–40 kHz. Other equipment used includes mass flow controllers (Alicat, MC-10SLPM-D), a tube furnace (BEQ, BTF-1200C-MS), and an industrial water chiller (S&A CW-3000) with 10 SLM water flow at the setting temperature of 20 °C. The reactor wall temperature was measured by an infrared thermometer (RS PRO TG301 Infrared Thermometer, Max Temperature +650 °C, ±3 °C).

DFT calculations: The structure relaxation and electronic structure calculations were performed using the Castep software with the GGA and PBE functions in the Material Studio package.[47,48] The convergence criterion for energy, maximum force, stress, and energy cutoff were set at 2×10^{-5} eV $atom^{-1}$, 0.05 eV $Å^{-1}$, 0.1 GPa, and 380 eV, respectively. Density mixing electronic minimizer with the mixing scheme of Pulay was used and the convergence criterion for self-consistent field (SCF) was set as 1.0×10^{-5} eV $atom^{-1}$. The Brillouin zone was sampled by k point of $2 \times 2 \times 1$. Moreover, the transition states (TS) were searched using the complete linear synchronous transit/quadratic synchronous transit (LST/QST) method for reactions,[49] and the convergence criterion was set to root mean square force on an atom below 0.25 eV $Å^{-1}$.[50]

All calculations of the energies and geometric optimizations consider the impact of spin polarization. Herein, a three-layer MgO(100) slab with a p(3 × 3) supercell was built and the positions of all atoms except for those in the bottom layer were fully relaxed. For Al_2O_3 support, a three-layer Al_2O_3(440) slab with a p (3 × 3) supercell was built and in the case of the SiO_2 support, a two-layer SiO_2(001) slab with a p(2 × 2) supercell was built. Considering the excellent activities of Ru/MgO catalyst, in this article, a Ru cluster containing 4 Ru atoms adsorbed on the center of MgO(100) surface was optimized. Due to the much lower deformation energies of Ru-MgO in NH_3 synthesis in comparison with adsorption energies, the atomic coordinates of Ru atoms were fixed during the NH_3 synthesis in order to reduce the time cost. For both structures, a vacuum of 12 Å along the Z direction was applied to avoid interactions between periodic images.

Adsorption energy was calculated as:

$$E_{ads} = E_{adsorbates/slab} - E_{slab} - E_{adsorbates} \qquad (6)$$

where $E_{adsorbates/slab}$, E_{slab}, and $E_{adsorbates}$ are the energies of the surface with the adsorbate molecule, clean surface without any adsorbate, and the isolated molecule in the gas phase, respectively.

The activation barrier E_a and reaction energy ΔE are defined as:

$$E_a = E(TS) - E(IS) \qquad (7)$$

$$\Delta E = E(FS) - E(IS) \qquad (8)$$

where $E(IS)$, $E(TS)$, and $E(FS)$ refer to the total energies of the initial, transition, and final states, respectively.

Plasma chemistry model: A zero-dimensional plasma chemistry model was used to simulate plasma-catalytic synthesis of ammonia in N_2/H_2O system at atmospheric pressure using ZDPlaskin.[51] The model includes ground states, vibrationally and electronically excited states molecules, radicals and ions of N_2, H_2O, as shown in Table S1 below. Detailed vibrational kinetics of 21 vibrationally excited states of $N_2(X, v)$ are considered with V-V' (vibrational–vibrational) energy exchange and V-T (vibrational–translational) interaction. Surface adsorption of gas-phase species and E-R (Eley–Rideal) interactions between gas species and surface-adsorbed species, and L-H (Langmuir–Hinshelwood) interaction between pairs of surface-adsorbed species are included as in the previous publications.[27,36] The input parameters are consistent with those in Figures S2, S3, and Figure S12A, while the activation energy of N_2 dissociation and adsorbed $NH_{x(x = 0,1,2)}$ hydrogenation is from Figure 3c and Figure S14.

The important gas-phase and surface reactions for the production and loss of H_2O, N_2, $N_2(A3)$, and NH_3 are shown in Figure S16. H_2O molecules are efficiently dissociated by electrons and excited $N_2(A_3)$ molecules where the nitrogen species is predominant. It is also confirmed that the vibrational excitation is the predominant pathway of power dissipation of electrons for both N_2 and H_2O molecules at this given plasma condition. It is worthwhile to note that OH radicals and hydrogen and oxygen atoms from H_2O are actively involved in the plasma chemistry in the N_2/H_2O system. They can be involved in the production or loss mechanisms of NH_3 and other heavy molecules such as NO_x. A significant amount of NH_3 is produced by the E-R mechanisms, such as $H_2 + NH(s)$, $NH_2 + H(s)$, and $H + NH_2(s)$, and the contribution of L-H mechanism turns out to be less important as shown in Figure S16D.

Conflict of Interest

The authors declare no conflict of interest.

Supporting Information

Supporting Information is available from the Wiley Online Library or from the author.

[1] D. R. MacFarlane, P. V. Cherepanov, J. Choi, B. H. Suryanto, R. Y. Hodgetts, J. M. Bakker, F. M. F. Vallana, A. N. Simonov, *Joule* **2020**, *4*, 1186.

[2] B. H. Suryanto, K. Matuszek, J. Choi, R. Y. Hodgetts, H.-L. Du, J. M. Bakker, C. S. Kang, P. V. Cherepanov, A. N. Simonov, D. R. MacFarlane, *Science* **2021**, *372*, 1187.

[3] F. Jiao, B. Xu, *Adv. Mater.* **2018**, *31*, e1805173.

[4] L. Wang, M. Xia, H. Wang, K. Huang, C. Qian, C. T. Maravelias, G. A. Ozin, *Joule* **2018**, *2*, 1055.

[5] J. G. Chen, R. M. Crooks, L. C. Seefeldt, K. L. Bren, R. M. Bullock, M. Y. Darensbourg, P. L. Holland, B. Hoffman, M. J. Janik, A. K. Jones, M. G. Kanatzidis, P. King, K. M. Lancaster, S. V. Lymar, P. Pfromm, W. F. Schneider, R. R. Schrock, *Science* **2018**, *360*, eaar6611.

[6] A. J. Martín, T. Shinagawa, J. Pérez-Ramírez, *Chem.* **2019**, *5*, 263.

[7] J. Sun, D. Alam, R. Daiyan, H. Masood, T. Zhang, R. Zhou, P. J. Cullen, E. C. Lovell, A. R. Jalili, R. Amal, *Energy Environ. Sci.* **2021**, *14*, 865.

[8] J. Wang, L. Yu, L. Hu, G. Chen, H. Xin, X. Feng, *Nat. Commun.* **2018**, *9*, 1.

[9] R. Hawtof, S. Ghosh, E. Guarr, C. Xu, R. M. Sankaran, J. N. Renner, *Sci. Adv.* **2019**, *5*, eaat5778.

[10] J. Zheng, Y. Lyu, M. Qiao, R. Wang, Y. Zhou, H. Li, C. Chen, Y. Li, H. Zhou, S. Wang, *Chem.* **2019**, *5*, 617.

[11] P. Mehta, P. Barboun, F. A. Herrera, J. Kim, P. Rumbach, D. B. Go, J. C. Hicks, W. F. Schneider, *Nat. Catal.* **2018**, *1*, 269.

[12] L. R. Winter, B. Ashford, J. Hong, A. B. Murphy, J. G. Chen, *ACS Catal.* **2020**, *10*, 14763.

[13] L. Hollevoet, F. Jardali, Y. Gorbanev, J. Creel, A. Bogaerts, J. A. Martens, *Angew. Chem. Int. Ed.* **2020**, *132*, 24033.

[14] E. C. Neyts, K. Ostrikov, M. K. Sunkara, A. Bogaerts, *Chem. Rev.* **2015**, *115*, 13408.

[15] X. Zhang, Y. Liu, M. Zhang, T. Yu, B. Chen, Y. Xu, M. Crocker, X. Zhu, Y. Zhu, R. Wang, *Chem.* **2020**, *6*, 3312.

[16] A. Bogaerts, E. C. Neyts, *ACS Energy Lett.* **2018**, *3*, 1013.

[17] P. Peng, C. Schiappacasse, N. Zhou, M. Addy, Y. Cheng, Y. Zhang, K. Ding, Y. Wang, P. Chen, R. Ruan, *Chemsuschem* **2019**, *12*, 3702.

[18] Z. Zhou, Z. Pei, L. Wei, S. Zhao, X. Jian, Y. Chen, *Energy Environ. Sci.* **2020**, *13*, 3185.

[19] R. K. Sharma, H. Patel, U. Mushtaq, V. Kyriakou, G. Zafeiropoulos, F. Peeters, S. Welzel, M. C. van de Sanden, M. N. Tsampas, *ACS Energy Lett.* **2020**, *6*, 313.

[20] I. Muzammil, Y.-N. Kim, H. Kang, D. K. Dinh, S. Choi, C. Jung, Y.-H. Song, E. Kim, J. M. Kim, D. H. Lee, *ACS Energy Lett.* **2021**, *6*, 3004.

[21] E. Carrasco, M. Jiménez-Redondo, I. Tanarro, V. J. Herrero, *Phys. Chem. Chem. Phys.* **2011**, *13*, 19561.

[22] X. Zhu, X. Hu, X. Wu, Y. Cai, H. Zhang, X. Tu, *J. Phys. D* **2020**, *53*, 164002.

[23] Y. Wang, M. Craven, X. Yu, J. Ding, P. Bryant, J. Huang, X. Tu, *ACS Catal.* **2019**, *9*, 10780.

[24] B. S. Patil, A. S. Van Kaathoven, F. J. Peeters, N. Cherkasov, J. Lang, Q. Wang, V. Hessel, *J. Phys. D* **2020**, *53*, 144003.

[25] C. Verheyen, T. Silva, V. Guerra, A. Bogaerts, *Plasma Sources Sci. Technol.* **2020**, *29*, 095009.

[26] K. H. Rouwenhorst, Y. Engelmann, K. van't Veer, R. S. Postma, A. Bogaerts, L. Lefferts, *Green Chem.* **2020**, *22*, 6258.

[27] J. Hong, S. Prawer, A. B. Murphy, *ACS Sustain. Chem. Eng.* **2018**, *6*, 15.

[28] B. Gordiets, C. Ferreira, M. Pinheiro, A. Ricard, *Plasma Sources Sci. Technol.* **1998**, *7*, 363.

[29] K. H. Rouwenhorst, H.-H. Kim, L. Lefferts, *ACS Sustain. Chem. Eng.* **2019**, *7*, 17515.

[30] F. Y. Hansen, N. E. Henriksen, G. D. Billing, A. Guldberg, *Surf. Sci.* **1992**, *264*, 225.

[31] A. Michaelides, A. Alavi, D. King, *J. Am. Chem. Soc.* **2003**, *125*, 2746.

[32] M. Kitano, S. Kanbara, Y. Inoue, N. Kuganathan, P. V. Sushko, T. Yokoyama, M. Hara, H. Hosono, *Nat. Commun.* **2015**, *6*, 1.

[33] K.-I. Aika, T. Takano, S. Murata, *J. Catal.* **1992**, *136*, 126.

[34] F. Rosowski, A. Hornung, O. Hinrichsen, D. Herein, M. Muhler, G. Ertl, *Appl. Catal. A Gen.* **1997**, *151*, 443.

[35] M. Muhler, F. Rosowski, O. Hinrichsen, A. Hornung, G. Ertl, *Stud. Surf. Sci. Catal.* **1996**, *101*, 317.

[36] J. Hong, S. Pancheshnyi, E. Tam, J. J. Lowke, S. Prawer, A. B. Murphy, *J. Phys. D* **2017**, *50*, 154005.

[37] J. Shah, W. Wang, A. Bogaerts, M. L. Carreon, *ACS Appl. Energy Mater.* **2018**, *1*, 4824.

[38] Y. Gorbanev, E. Vervloessem, A. Nikiforov, A. Bogaerts, *ACS Sustain. Chem. Eng.* **2020**, *8*, 2996.

[39] P. Peng, P. Chen, M. Addy, Y. Cheng, Y. Zhang, E. Anderson, N. Zhou, C. Schiappacasse, R. Hatzenbeller, L. Fan, *ChemComm.* **2018**, *54*, 2886.

[40] J. R. Toth, N. H. Abuyazid, D. J. Lacks, J. N. Renner, R. M. Sankaran, *ACS Sustain. Chem. Eng.* **2020**, *8*, 14845.

[41] T. Sakakura, S. Uemura, M. Hino, S. Kiyomatsu, Y. Takatsuji, R. Yamasaki, M. Morimoto, T. Haruyama, *Green Chem.* **2018**, *20*, 627.

[42] T. Haruyama, T. Namise, N. Shimoshimizu, S. Uemura, Y. Takatsuji, M. Hino, R. Yamasaki, T. Kamachi, M. Kohno, *Green Chem.* **2016**, *18*, 4536.

[43] H. H. Kim, Y. Teramoto, A. Ogata, H. Takagi, T. Nanba, *Plasma Process. Polym.* **2017**, *14*, 1600157.

[44] V. Kyriakou, I. Garagounis, A. Vourros, E. Vasileiou, M. Stoukides, *Joule* **2020**, *4*, 142.

[45] J. J. Wang, L. T. Zhang, Q. F. Zeng, G. L. Vignoles, L. F. Cheng, A. Guette, *Phys. Rev. B* **2009**, *79*, 125304.

[46] Y. T. Gong, J. Z. Wu, M. Kitano, J. J. Wang, T. N. Ye, J. Li, Y. Kobayashi, K. Kishida, H. Abe, Y. Niwa, H. S. Yang, T. Tada, H. Hosono, *Nat. Catal.* **2018**, *1*, 178.

[47] M. C. Payne, M. P. Teter, D. C. Allan, T. Arias, A. J. Joannopoulos, *Rev. Mod. Phys.* **1992**, *64*, 1045.

[48] B. Delley, *J. Phys. Chem.* **1996**, *100*, 6107.

[49] T. Halgren, W. Lipscomb, *Phys. Lett.* **1977**, *49*, 225.

[50] Z. Han, Z. Yang, M. Han, *Appl. Surf. Sci.* **2019**, *480*, 243.

[51] S. Pancheshnyi, B. Eismann, G. Hagelaar, L. Pitchford, Tech. Rep., CNRS-UPS-INP, Toulouse, France **2008**.